PTE effect can also demonstrate the photoresponse in graphene–metal interfaces. It has been shown theoretically that the difference in the Fermi-level positions within a graphene layer can also generate a PTE effect. By avoiding the direct heat transfer to the substrate, a large PTE effect can be observed in suspended graphene with a responsivity of ~10 mA W^{-1} and an IQE of ~40% [15]. Fast photoresponse switching speeds of more than 60 GHz is demonstrated in graphene-based PTE photodetectors. Here, we discuss to further understand the physical properties and parameters involved in the PTE effect in graphene.

The heat transport in the device strongly influences both the efficiency and response time of the device. Under pulsed excitation, we can estimate the response time based on the initial rise in temperature $\Delta T_e(t)$ and the cooling time τ_{cool} as

$$\Delta T_e(t) = \Delta T_e(0)\exp\left(-t/\tau_{\text{cool}}\right) \tag{1.10}$$

Here, the characteristic cooling time, $\tau_{\text{cool}} = C_e/\Gamma$, where C_e is the electronic heat capacity, and Γ is a proportionality constant. When the system comes to a steady-state condition,

$$\Delta T = \frac{P_{\text{in}}}{\Gamma} = \frac{P_{\text{in}}\tau_{\text{cool}}}{C_e} \tag{1.11}$$

We can express the photocurrent under pulsed excitation as

$$I_P = \frac{\Delta S}{R}\frac{P_{\text{in}}\tau_{\text{cool}}}{C_e} \tag{1.12}$$

Based on this, the IQE (η_i) can be expressed as

$$\eta_i = \frac{h\nu}{eA}\frac{\Delta S}{R}\frac{P_{\text{in}}\tau_{\text{cool}}}{C_e} \tag{1.13}$$

Graphene is an excellent PTE material with very low C_e and very large S close to the Dirac point. If the carrier mobility is independent of the position of the Fermi level, then we can estimate the Seebeck coefficient of graphene with the Mott formula,

$$S = -\frac{2\pi^2 k_B^2 T_e}{3e_0 E_F} \tag{1.14}$$

The above equation indicates that S increases with decreasing E_F. But this analogy cannot be applied if $k_B T_e >> E_F$.

In graphene PTE photodetectors, based on the differences in the Fermi-level positions, a sixfold pattern of photocurrent can be observed that helps to distinguish it from the PV effect. The PTE effect in graphene with sixfold pattern of photoresponse is clearly evident in a single-layer graphene (SLG) connected by source (S) and drain (D) contacts and dual gates where the top gate is separated by the h-BN layer, and the bottom gate by SiO_2, as shown in Figure 1.5. It has been verified that the PTE current becomes zero when there is no difference between the positions of Fermi levels in

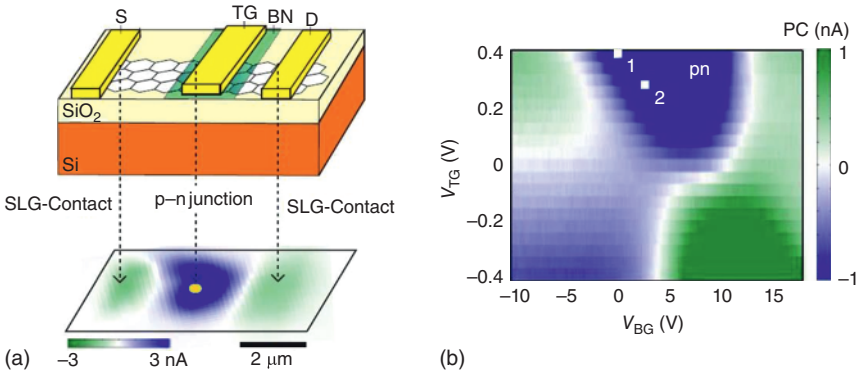

Figure 1.5 Photothermionic effect in graphene-based device. (a) Schematic of single-layer graphene (SLG) connected by source (*S*) and drain (*D*) contacts and dual gates where the top gate is separated by the h-BN layer, and the bottom gate by SiO_2. (b) Photocurrent mapping by varying top and bottom gating at the position of yellow mapping in the panel in (a). Source: Mathieu [8]/CC BY SA 4.0.

the two regions. Unlike the PV effect, electrons and holes contribute to the PTE effect and cancel each other. In the PV case, the polarity of photocurrent changes only once when both Fermi levels are equal. In graphene-based PTE photodetectors, there is always a trade-off between performance metrics such as IQE and the relaxation time based on the cooling time. For instance, long cooling times give higher IQE but with lower response times. The relaxation of hot carriers in graphene depends on various relaxation pathways, and in general, the cooling times are ~1 ps, implying large theoretical bandwidth of ~500 GHz and IQE within 20% [7, 16, 17]. Graphene with almost uniform optical absorption from MIR to UV region is highly promising in designing broadband photodetectors based on the PTE effect.

1.4.5.2 Photobolometric Effect (PBE)

When the transport conductance (G_e) of material changes due to heating induced by the photon absorption,

$$I_{\mathrm{PC}} = \frac{\partial G_e}{\partial T} V \Delta T_e \tag{1.15}$$

One of the crucial differences between PTE and photobolometric effect (PBE) is that the photoinduced heat modifies the transport properties of the material rather than the transport of charge carriers, as in the case of the PTE effect. In this case, the conductivity change is due to the carrier mobility's dependence on temperature. So, unlike the PTE effect, external bias is required to drive the photocurrent in PBE and can emerge in homogeneous materials without a junction. The photoresponse time of the PB effect is very similar to the PTE effect as they both rely on the cooling of the hot electrons. Several studies have investigated the PBE in graphene and other 2D materials [18–20]. However, the responsivities reported in these studies are relatively low (~0.2 mA W^{-1}) compared with PTE-based devices.

1.4.5.3 Photothermionic (PTI) Effect

Ever since the discovery of the photoelectric effect, the emission of electrons from a solid by the absorption of photons, gaining importance both in terms of fundamental physics and real-world applications. Schottky junction provides a simple device scheme to photoelectric effect with the emission of photoexcited electrons into another material, known as internal photoemission (IPE). This IPE led to the development of visible to infrared photodetectors [21, 22]. However, the efficiency of these devices drops sharply if the photon energy drops lower than the interfacial barrier height. Thermalized carriers or hot electrons, via electron–electron scattering, increase the transfer efficiency of IPE by raising a fraction of electrons above the interfacial barrier. This phenomenon, generally called the PTI effect [23, 24], is inefficient in metals due to strong electron–phonon interaction. High thermal conductivity instantly brings electrons to thermal equilibrium with the surroundings in ~100 fs. Choosing a photoabsorber with a weak electron–phonon interaction can hold most of the absorbed photon energy within the electronic system, resulting in a large population of hot electrons with energies much higher than that of direct transitions. There is a promising approach to photodetection of photon energies much lower than the Schottky barrier height. By choosing a material where hot carriers are weakly coupled with the surrounding phonon bath, such as graphene [23, 24], thermalization of photoexcited carriers with other carriers results in hot carrier distribution with a well-defined temperature, T_e [25, 26]. Realizing sufficient T_e that can overcome the Schottky barrier height, a large pool of electrons that can be emitted as photon energies much lower than the barrier height can still contribute to the hot electron distribution and thus lead to the photocurrent over the barrier.

1.4.5.4 Photogating Effect

Low-intensity light detection, even when the detection limit approaches the single-photon level, requires a gain mechanism for photocurrent generation where a single-photon absorption gives multiple carriers. Photogating is one such approach for gain in photodetectors. Instead of being used as a light-absorbing medium, graphene can also play a role as a transparent, high carrier mobility channel material and sense the photogenerated carriers in the adjacent semiconducting absorber, thus extending the operational bandwidth to midinfrared with high-performance metrics. In graphene-based phototransistors, the principle of photogate is the detection of change in resistance of graphene with the corresponding light-induced change in the substrate potential. The photogate effect can leverage the large transconductance of graphene-based transistors. In this case, graphene is capacitively coupled to the substrate, and the evolution of photogenerated carriers in the substrate reflects in the conductivity of graphene. For this, the photon energy of the detected radiation must be higher than the bandgap of the semiconductor substrate that generates electron–hole pairs and separates into different zones by the electric field. These separated charges appear at the semiconductor's surface and alter the effective chemical potential in the substrate. Due to capacitive coupling, this change in chemical potential in the substrate reflects in the charge carrier density with

opposite polarity in graphene. The resultant voltage on the graphene–oxide–semiconductor (GOS) structure [27] can be represented as

$$eV_g = eFd + \Delta\mu_{gr} - \Delta\mu_{Si} \approx eFd = 4\pi e^2 nd\frac{1}{\varepsilon} \tag{1.16}$$

Here, V_g is the gate voltage, F is the electric field between the substrate and graphene, d is the thickness of the oxide, $\mu_{gr,\,Si}$ is the chemical potential of graphene and silicon, n is the excess interface charge density, and ε is the dielectric constant.

To further improve the sensitivity of this device scheme, the substrate is kept in a nonequilibrium deep-depletion state, which significantly improves the photogenerated electron–hole pair separation and holds one type of charge that capacitively couples with the opposite charge in the graphene channel [28]. In this concept, to detect the photogenerated carriers, the semiconductor in a GOS device is kept in deep depletion by rapid application of back-gate voltage. The energy band diagram of GOS device with n-type Si biased in the deep-depletion state is depicted in Figure 1.6. Positive gate voltage drives mobile electrons into the bulk Si and space charge into the deep-depletion region of width W. The depletion region separates the electron–hole pairs, and the holes collect at the silicon–oxide interface as the surface potential goes negative. As the graphene capacitively couples with the Si

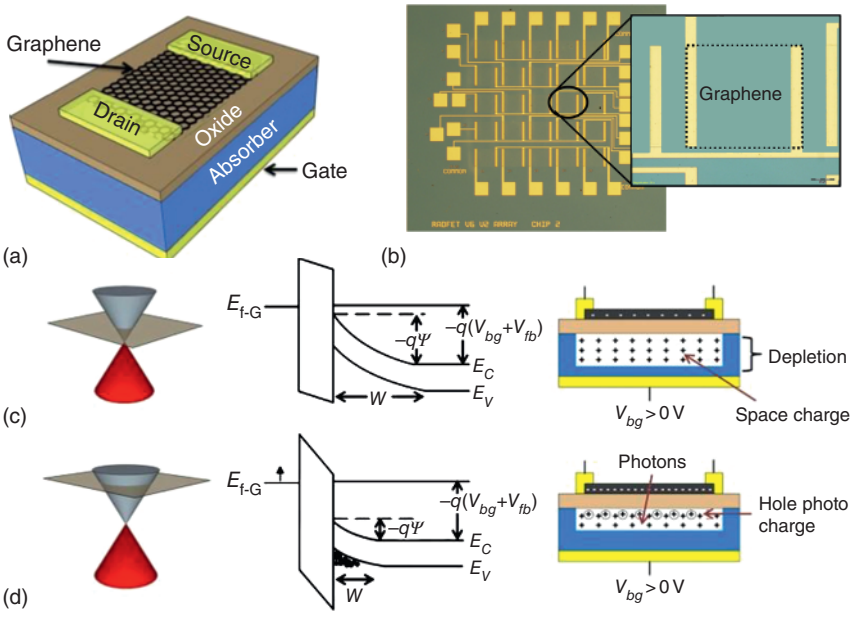

Figure 1.6 Deep-depletion GOS device and operating principle. (a) Schematic of the GOS device. (b) Optical image of several GOS devices integrated in an Si/SiO_2 substrate. (c) Band diagram of GOS device in the deep-depletion state. $E_{f\text{-}G}$ is the Fermi level of graphene, and the combination of both gate and channel bias ($V_{bg} + V_{fb}$) acting on the band bending near the interface, assuming lightly n-doped silicon. (d) Under illumination, a large density of holes accumulates in the interface inducing a negative charge and thus the n-type doping and Fermi-level shift in graphene. Source: Howell et al. [28]; Springer Nature/CC BY 4.0.

substrate, holes collected at the interface induce electrons in the graphene channel and modify the Fermi level reflected in the channel conductivity. This change in conductivity can be sensed from the drain–source current when a slight bias is applied. This phenomenon is well described in Figure 1.6. Here, it is worth noting that the deep-depletion state occurs when the gate voltage sweep is fast enough to avoid the formation of the inversion layer or if the device cannot maintain thermal equilibrium [27, 28]. The rate of gate voltage change can be expressed with the relation,

$$\frac{dV_g}{dt} \gg \frac{qn_i}{2C_{\text{ox}}}\sqrt{\frac{\mu_{\text{Si}}V_t}{\tau_p}} \tag{1.17}$$

where V_g is the gate voltage, n is the interface charge density, V_t is the thermal voltage (~26 mV), C_{ox} is the oxide capacitance, and τ_p is the minority carrier lifetime. For lightly doped Si (N_d ~$9\times10^{13}\text{cm}^{-3}$), the typical $\frac{dV_g}{dt}$ values are ~$0.8\,\text{V}\,\text{s}^{-1}$.

There is another approach for the photogate effect in graphene with an absorber material such as quantum dots (QDs), semiconductors, and pyroelectric materials. Since the role of graphene in these detectors is only charge sensing, the choice of the absorber decides the spectral response [29–31]. Therefore, this device concept is equally applicable and suitable for detecting infrared to ionizing radiation. The sensitivity of this photodetector is determined by both the transconductance of the graphene and the generation recombination of the absorber. Thus, the full functionality of the device can be realized only when graphene and the absorber are incorporated into a single device, as shown in Figure 1.7a. The key response of the device is the shift in the channel resistance versus the gate voltage, as shown in Figure 1.7b. The short carrier transit time reflected in the fast response time makes graphene an

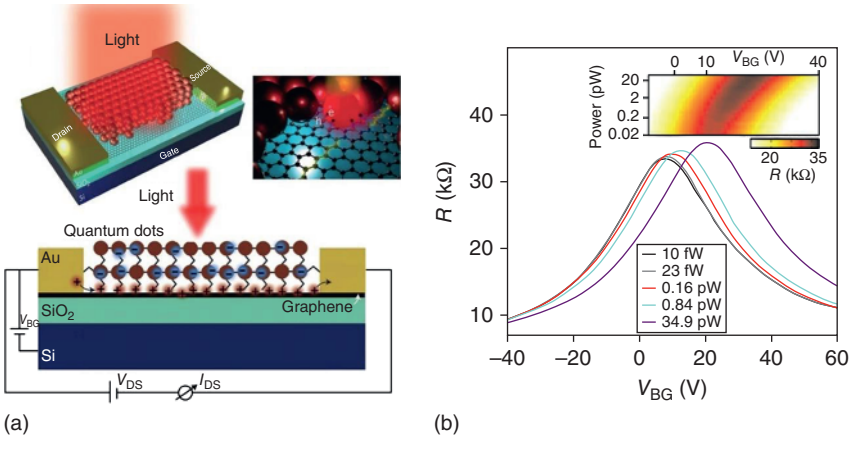

Figure 1.7 (a) Schematic of a graphene-quantum dot hybrid phototransistor. (b) Channel resistance versus gate voltage of the graphene-quantum dot hybrid phototransistor. Source: Reproduced with permission from Konstantatos et al. [29]; Springer Nature.

excellent material for high-gain photodetection at room temperature [29]. Some of these light-absorbing particles showing favorable responses in sensitizing graphene are colloidal QDs made of PbS, ZnO, and CdS [29–31]. By varying the size of these quantum detectors, strong light absorption and bandgap tunability can be achieved along with spectral response range from UV to short-wave infrared (SWIR). Another advantage of these QDs is the easy integration as they can be processed in solution and deposited by spin-coating, ink-jet-printing, and contact-printing techniques. In addition, the surface of these particles can be optimized for efficient charge transfer within QDs or with graphene. Large QE values >25% have been demonstrated in these hybrid photodetectors.

1.4.6 Infrared Modulators

Integrating with other materials is inevitable to extend the operational bandwidth of Si modulators into the midinfrared region. With its straightforward CMOS foundry-compatible processing, graphene became a viable choice for IR modulators. Based on the Fermi-level dependence of the optical absorption in graphene, several graphene-Si waveguide-integrated IR modulators have been demonstrated. The working principles of these modulators are simply based on tuning the optical absorbance in graphene by varying the Fermi-level dependence of the optical absorption in graphene. For instance, in graphene waveguide-integrated optical modulators, graphene is placed on Si/SiO_2 ridge waveguide where Si is used to electrostatically tune the Fermi-level position in graphene (Figure 1.8a,b). The waveguide is designed explicitly for the operation at 1.53 μm wavelength, and most of the optical mode intensity lies in the graphene/SiO_2 region [32].

The blue dotted lines in Figure 1.8c in both the valence and conduction bands of graphene indicate the incident photon energy range where Fermi level can be tuned with applied gate bias or drive voltage from below to above the two lines. If E_F is placed below the blue bottom line, there are no available electrons for interband transition, giving the lower absorption. When the Fermi level rises above the blue bottom line, the optical absorption increases gradually and decreases when E_F approaches the top dotted blue line. If the E_F crosses the top blue line, then there are no available states to transfer the electrons in the conduction band; thus, the absorption is dropped. This is depicted in the transmission versus drive voltage plot in Figure 1.8c. The switching speed of these modulators is ~1 GHz, which is mainly limited by the RC time constant. With this device structure, modulation of ~0.09 $dB\,\mu m^{-1}$ can be achieved [32]. The optical absorption can be increased by systematically increasing the number of graphene layers, where the configurable regions with graphene–insulator–graphene structures demonstrated modulation depth of ~0.16 $dB\,\mu m^{-1}$.

1.4.7 Photovoltaic Devices

Converting light to electricity is the primary function of a photovoltaic cell. The energy conversion efficiency can be defined as $\eta = P_{max}/P_{in}$ and can also be represented as

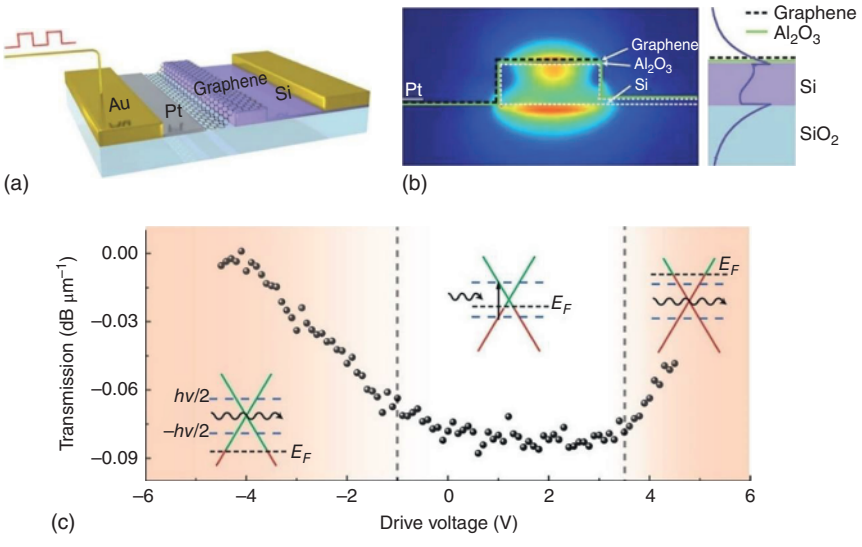

Figure 1.8 (a) 3D sketch of graphene-integrated Si waveguide optical modulator. (b) Cross section of the device with the optical mode overlay. (c) Optical transmission as a function of the drive voltage. Source: Liu et al. [32]; Springer Nature.

$$\eta = \frac{V_{OC} \times I_{SC} \times FF}{P_{in}} \tag{1.18}$$

Here, FF is the fill factor and defined as $FF = \frac{V_{Max} \times I_{MAX}}{V_{OC} \times I_{SC}}$, and V_{OC} is the maximum open-circuit voltage. V_{Max} and I_{MAX} are the maximum voltage and current values. Similar to photodetectors, the fraction of absorbed photons converted to current defines the internal photocurrent efficiency. Graphene can fulfill many roles in photovoltaic devices as transparent conductive window, charge transport channel, and the broadband photoabsorbing material. Graphene and its derivatives have been used as transparent electrodes in inorganic, organic, and dye-sensitized solar cells [33, 34]. The present photovoltaic market is strongly dominated by silicon-based solar cells with a maximum quantum efficiency of ~25% [4]. Even though the quantum efficiencies of these solar cells are much lower than the silicon solar cells, fabrication costs can be significantly minimized as they can be prepared in a roll-to-roll process.

1.5 Outlook

Heat transduction into electrical energy is pivotal in designing next-generation miniaturized electronics. Distributing the absorbed photon energy within the electron bath and effectively transporting it out of the system is an essential but challenging task that must be addressed with emerging materials and device schemes. Graphene with weak electron–phonon coupling provides an ideal platform to harness

excessive heat in the electronic system. The vertical and lateral graphene-bulk (3D) semiconductor heterostructures open a reliable path to commercialization while enabling a testbed to explore hot electron-based transport from graphene to 3D systems. Therefore, future research needs to be focused on developing large-scale, CMOS-compatible graphene-Si optoelectronic devices suitable for a wide range of applications discussed above with room temperature operation.

References

1 Castro Neto, A.H., Guinea, F., Peres, N.M.R. et al. (2009). The electronic properties of graphene. *Reviews of Modern Physics* 81 (1): 109–162.
2 Akinwande, D., Huyghebaert, C., Wang, C.-H. et al. (2019). Graphene and two-dimensional materials for silicon technology. *Nature* 573 (7775): 507–518.
3 Ferrari, A.C., Bonaccorso, F., Fal'ko, V. et al. (2015). Science and technology roadmap for graphene, related two-dimensional crystals, and hybrid systems. *Nanoscale* 7 (11): 4598–4610.
4 Bonaccorso, F., Sun, Z., Hasan, T., and Ferrari, A.C. (2010). Graphene photonics and optoelectronics. *Nature Photonics* 4 (9): 611–622.
5 Sensale-Rodriguez, B. (2015). Graphene-based optoelectronics. *Journal of Lightwave Technology* 33 (5): 1100–1108.
6 Kampfrath, T., Perfetti, L., Schapper, F. et al. (2005). Strongly coupled optical phonons in the ultrafast dynamics of the electronic energy and current relaxation in graphite. *Physical Review Letters* 95 (18): 187403.
7 Koppens, F.H.L., Mueller, T., Avouris, P. et al. (2014). Photodetectors based on graphene, other two-dimensional materials and hybrid systems. *Nature Nanotechnology* 9 (10): 780–793.
8 Mathieu, M. (2017). *Ultrafast Optoelectronics in 2D Materials and Their Heterostructures*. Universitat Politècnica de Catalunya.
9 Peters, E.C., Lee, E.J.H., Burghard, M., and Kern, K. (2010). Gate dependent photocurrents at a graphene p–n junction. *Applied Physics Letters* 97 (19): 193102.
10 Lemme, M.C., Koppens, F.H.L., Falk, A.L. et al. (2011). Gate-activated photoresponse in a graphene p–n junction. *Nano Letters* 11 (10): 4134–4137.
11 Ang, Y.S., Cao, L., and Ang, L.K. (2021). Physics of electron emission and injection in two-dimensional materials: theory and simulation. *InfoMat* 3 (5): 502–535.
12 Gabor, N.M., Song, J.C.W., Ma, Q. et al. (2011). Hot carrier assisted intrinsic photoresponse in graphene. *Science* 334 (6056): 648–652.
13 Mueller, T., Xia, F., and Avouris, P. (2010). Graphene photodetectors for high-speed optical communications. *Nature Photonics* 4 (5): 297–301.
14 Gan, X., Shiue, R.-J., Gao, Y. et al. (2013). Chip-integrated ultrafast graphene photodetector with high responsivity. *Nature Photonics* 7 (11): 883–887.
15 Freitag, M., Low, T., and Avouris, P. (2013). Increased responsivity of suspended graphene photodetectors. *Nano Letters* 13 (4): 1644–1648.
16 Xia, F., Mueller, T., Lin, Y.-m. et al. (2009). Ultrafast graphene photodetector. *Nature Nanotechnology* 4 (12): 839–843.

17 Shiue, R.-J., Gao, Y., Wang, Y. et al. (2015). High-responsivity graphene–boron nitride photodetector and autocorrelator in a silicon photonic integrated circuit. *Nano Letters* 15 (11): 7288–7293.

18 Schuler, S., Schall, D., Neumaier, D. et al. (2016). Controlled generation of a p–n junction in a waveguide integrated graphene photodetector. *Nano Letters* 16 (11): 7107–7112.

19 Freitag, M., Low, T., Xia, F., and Avouris, P. (2013). Photoconductivity of biased graphene. *Nature Photonics* 7 (1): 53–59.

20 Yan, J., Kim, M.H., Elle, J.A. et al. (2012). Dual-gated bilayer graphene hot-electron bolometer. *Nature Nanotechnology* 7 (7): 472–478.

21 Scales, C. and Berini, P. (2010). Thin-film Schottky barrier photodetector models. *IEEE Journal of Quantum Electronics* 46 (5): 633–643.

22 Emmanuel Rosencher, B.V. (2002). *Optoelectronics*. Cambridge: Cambridge University Press.

23 Massicotte, M., Schmidt, P., Vialla, F. et al. (2016). Photo-thermionic effect in vertical graphene heterostructures. *Nature Communications* 7 (1): 12174.

24 Massicotte, M., Schmidt, P., Vialla, F. et al. (2016). Picosecond photoresponse in van der Waals heterostructures. *Nature Nanotechnology* 11 (1): 42–46.

25 Tielrooij, K.J., Piatkowski, L., Massicotte, M. et al. (2015). Generation of photovoltage in graphene on a femtosecond timescale through efficient carrier heating. *Nature Nanotechnology* 10 (5): 437–443.

26 Massicotte, M., Soavi, G., Principi, A., and Tielrooij, K.-J. (2021). Hot carriers in graphene – fundamentals and applications. *Nanoscale* 13 (18): 8376–8411.

27 Voronin, K.V., Ermolaev, G.A., Stebunov, Y.V. et al. (2021). Photogating in graphene field-effect phototransistors: theory and observations. *AIP Conference Proceedings* 2359 (1): 020034.

28 Howell, S.W., Ruiz, I., Davids, P.S. et al. (2017). Graphene-insulator-semiconductor junction for hybrid photodetection modalities. *Scientific Reports* 7 (1): 14651.

29 Konstantatos, G., Badioli, M., Gaudreau, L. et al. (2012). Hybrid graphene–quantum dot phototransistors with ultrahigh gain. *Nature Nanotechnology* 7 (6): 363–368.

30 Sun, Z., Liu, Z., Li, J. et al. (2012). Infrared photodetectors based on CVD-grown graphene and PbS quantum dots with ultrahigh responsivity. *Advanced Materials* 24 (43): 5878–5883.

31 Guo, W., Xu, S., Wu, Z. et al. (2013). Oxygen-assisted charge transfer between ZnO quantum dots and graphene. *Small* 9 (18): 3031–3036.

32 Liu, M., Yin, X., Ulin-Avila, E. et al. (2011). A graphene-based broadband optical modulator. *Nature* 474 (7349): 64–67.

33 Junbo, W., Héctor, A., Zhenan, B. et al. (2011). Organic solar cells with solution-processed graphene transparent electrodes. *Applied Physics Letters* 92 (1): 2633021.

34 Lewis, G.D.A., Yi, Z., Cody, W.S. et al. (2010). Highly flexible, and transparent graphene films by chemical vapor deposition for organic photovoltaics. *ACS Nano* 4 (5): 2865–2873.